Appl. Phys. A 67, 29–37 (1998)

Applied Physics A
Materials
Science & Processing

Large-scale purification of single-wall carbon nanotubes: process, product, and characterization

A.G. Rinzler[1], J. Liu[1], H. Dai[1], P. Nikolaev[1], C.B. Huffman[1], F.J. Rodríguez-Macías[1], P.J. Boul[1], A.H. Lu[1], D. Heymann[1], D.T. Colbert[1], R.S. Lee[2], J.E. Fischer[2], A.M. Rao[3], P.C. Eklund[3], R.E. Smalley[1]

[1] Center for Nanoscale Science and Technology, Rice Quantum Institute, Departments of Chemistry and Physics, Rice University, Houston TX 77005, USA
[2] Department of Materials Science and Engineering and Laboratory for Research on the Structure of Matter, University of Pennsylvania, Philadelphia PA 19104-6272, USA
[3] Department of Physics and Astronomy and Center for Applied Energy Research, University of Kentucky, Lexington KY 40506-0055, USA

Received: 13 February 1998

Abstract. We describe, in detail, a readily scalable purification process capable of handling single-wall carbon nanotube (SWNT) material in large batches. Characterization of the resulting material by SEM, TEM, XRD, Raman scattering, and TGA shows it to be highly pure. Resistivity measurements on freestanding mats of the purified tubes are also reported. We also report progress in scaling up SWNT production by the dual pulsed laser vaporization process. These successes enable the production of gram per day quantities of highly pure SWNT, which should greatly facilitate investigation of material properties intrinsic to the nanotubes.

PACS: 81.15T; 72.80R; 61.48

In 1996, a dual pulsed laser vaporization (PLV) technique for the generation of single-wall carbon nanotubes (SWNT) was reported [1]. This produced 70–90 vol.% SWNT, organized in hexagonal close-packed bundles (ropes). As the result of prior theoretical predictions concerning their novel electronic properties [2] and anticipated extreme tensile strength, this finding led to a dramatically heightened interest and demand for this exciting new material. In an attempt to satisfy this demand the Rice group undertook to scale up SWNT production by the PLV process. This work revealed a high sensitivity of the material quality (fractional SWNT yield) to several parameters, some of which turn out to be incompatible, in an engineering sense, with large-scale production of the highest quality material. This compromise of raw-material quality for quantity required that a collateral battle be fought on the material purification front.

We report on a process developed for purification of large batches of SWNT material resulting in high-purity SWNT, essentially independent of the material starting quality. The purified SWNT material is characterized by electron microscopy, X-ray diffraction (XRD), Raman spectroscopy, and thermo-gravimetric analysis (TGA). Temperature-dependent resistivity measurements performed on freestanding mats of the purified tubes are also reported. Other techniques for purification of SWNT are found in the literature [3–5]. These all suffer from the problem that they are microscale techniques, of varying degrees of effectiveness, which have not proved useful for purifying large batches of moderate-quality material. The purification process reported here, in contrast, is a macroscale technique which may readily be scaled further to industrial levels of throughput when such volumes of SWNT material become available.

We additionally report on some observations concerning the differences in SWNT material made under distinct growth conditions encountered during the production scale-up. In particular, it is found, in corroboration of an independent (and significantly more systematic) investigation [6] of the phenomena, that the SWNT diameter distribution shifts to larger diameters when the vaporization and SWNT growth takes place at a higher surrounding background temperature.

1 SWNT material production

The limiting factor in the original 1″-flow-tube system (described previously [1]) was plugging of the tube around the target by the web-like SWNT deposit. The materials used in the present investigations were made in two different PLV systems which were successive scale-ups from the original apparatus. A description of each and the production conditions pertaining to the resulting material follows.

1.1 2″ *apparatus*

The first scale-up incorporated a 2″-diameter horizontal flow tube within a tube furnace held at elevated temperature and arranged to maintain an argon atmosphere flow at a controlled pressure. Laser pulses from two Spectra Physics GCR-250 lasers, each running at 30 Hz, entered the flow tube through a Brewster angle window on the front flange and propagated coaxially down the tube in the same direction as the Ar flow.

The target consisted of a 1″-diameter, 1″-long, right circular cylinder (Co/Ni, 1 at.% each, balance carbon) which was situated coaxially in the flow tube, within the furnace heated zone. In this arrangement the ablation occurred from one of the target's circular end faces. In order to utilize the target efficiently the laser pulses were rastered across the entire face. SWNTs condensing from the laser vaporization plume were entrained in the Ar flow to be swept downstream and deposit on the quartz tube walls outside the heated zone.

After optimizing parameters (laser powers, spot sizes, timing, gas flow rate, and pressure) it was found that generation of material containing > 50 vol.% SWNT required a modification which mimicked, in part, the geometry of the original 1″-flow-tube apparatus. This involved adding a 1″-diameter (1.3″ O.D.) quartz tube coaxial with the 2″ tube extending from the front flange to within 4 mm of the target face (Fig. 1). With this new configuration the vaporization plume now lifted off the target face to extend well into this inner tube such that the nucleation and much of the SWNT growth took place within the confines of this tube. Following this modification the material quality ranged from 60–90 vol.% SWNT (the remaining variation was due to differences in target porosity, density, and homogeneity). Whereas the original 1″ apparatus produced ≈ 80 mg/day, this 2″ apparatus was capable of generating ≈ 1 g/day.

A batch of 60–70 vol.% SWNT material made with this system provided samples for the studies below and is referred to as 2″ apparatus (or just 2″) material. Production conditions for this material were: 1200 °C, 100 sccm flowing argon, 500 Torr, first laser pulse 532 nm, 490 mJ/P, 6-mm-diameter spot, second laser pulse 1064 nm, 550 mJ/P, overlapping 6-mm spot with 42 nS delay between pulses.

Further scale-up required a more drastic departure from the original design. A common effect observed in long-term laser ablation is the development of faceted peaks on the target, which grow with increasing exposure time (even when the beam is rastered across the surface). Since the energy density impinging on a surface depends on the angle between the direction of propagation and the surface normal (viz. $\cos(\theta)$), the absorbed energy density decreases as the faceted sides of the peaks become steeper, until ultimately the energy density drops below the ablation threshold and vaporization is arrested. In the 2″ apparatus this condition was typically reached after 2–3 h of operation, which required that the apparatus be shut down, the target removed and re-faced, before being replaced in the apparatus to be pumped out, purged with Ar and brought back to 1200 °C for further production.

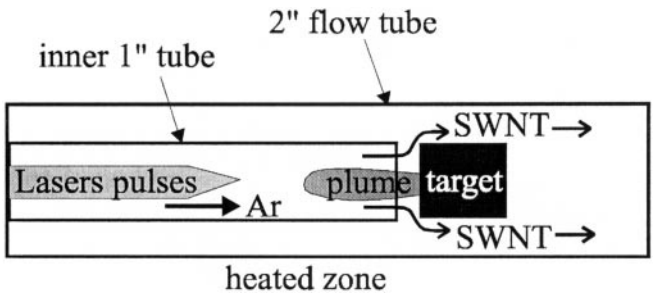

Fig. 1. The configuration in the 2″ system capable of giving a fractional SWNT yield comparable to that of the original 1″ system but at ≈ 1 g/day production rate

1.2 4″ apparatus

The common solution to the target pitting problem in laser ablation is to have the laser beam impinge on the surface from two distinct directions, each $\approx 15°$–$30°$ off the surface normal. This is not feasible within the confines of a flow tube furnace. Figure 2 shows the alternative solution we implemented. The laser beam is repetitively rastered up and down the cylindrical surface of the now vertical, rotating target (Fig. 2, side view). By periodically switching the side of the target which is ablated (Fig. 2, top view) the laser angle of attack is effectively changed such that the deep pitting which previously stopped the ablation is avoided.

Unfortunately, this solution was incompatible with an internal 1″-plume-expansion confinement tube since the vaporization plume would be aimed directly toward one or the other wall of the inner tube (the plume propagates normal to the target surface independent of the laser propagation direction) causing much of the vaporized carbon to condense as a graphitic coating on the confinement tube walls. Although the fractional SWNT yield without this tube is significantly lower, the advantage of long-term, unattended production affords a favorable trade-off.

This was further enhanced by adopting a 4″-I.D.-flow-tube system which, along with the thickness of the target rotation mechanism (all carbon, worm drive assembly to withstand the high temperature), can accommodate a 2″-long (initially 1″-diameter) vertical target. The larger diameter flow tube cannot tolerate sustained operation at 1200 °C, so SWNT production in this apparatus takes place at a furnace temperature of 1100 °C. With this system, dual laser pulses with the

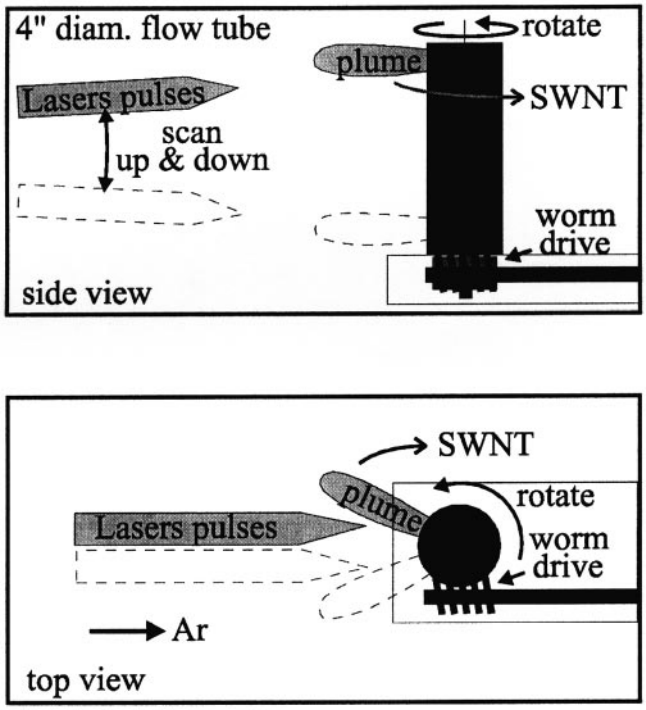

Fig. 2. The configuration in the 4″ system. The target rotates about its vertical axis. The laser beams are swept up and down one side of the target (*side view*) for several minutes before periodically being shifted to the other side of the target (*top view*), where they again sweep up and down the side of the target

initial pulse at a wavelength of 532 nm were found to have little advantage in the fractional SWNT yield compared with dual 1064-nm pulses. This obviated the need for constant tuning of the second-harmonic generation crystal to maintain the peak power of an initial 532-nm pulse. With these conditions (including 750 sccm Ar flow rate, 500 Torr, dual 1064-nm pulses, 930 mJ/P coincident on a 7.1-mm-diameter spot separated by a 40 nS delay) the 4″ apparatus is capable of generating 20 g of 40–50 vol.% SWNT material in 48 h of continuous, largely unattended, operation.

Material made in this system which was used in the following studies is referred to below as 4″ apparatus (or just 4″) material. This material was produced before production in this system was fully optimized. In particular, the lasers were more tightly focused to 6.8-mm-diameter spots. The resulting higher energy density had the effect of knocking large, $\approx 3\,\mu$m, graphite flakes off the target surface. These particles are not removed by the purification process described below and were evident in the XRD data. The lower energy density presently used in the more optimized process (7.1-mm-diameter spots) largely avoids this contaminant.

2 Purification

Purification begins with a 45-h reflux in 2–3 M nitric acid (typically 1 liter of acid per 10 g of raw material). Weight loss is $\approx$ 70% after 24 h with little further weight loss after this time. The ability of the nanotubes to survive such long-term, high-temperature exposure to a strongly oxidizing acid (known previously for multi-wall nanotubes [7]), is evidence of the chemical robustness of these structures.

Following the reflux the black solution is centrifuged ($20\,000 \times g$, 20 min, Sorvall, R5C) leaving a black sediment at the bottom of the centrifuge bottle and a clear, brownish-yellow supernatant acid, which is decanted off. The sediment still contains substantial trapped acid which is removed by repeatedly re-suspending the sediment in deionized water (by shaking vigorously), centrifuging, and decanting the supernatant liquid (for 10 g of starting material 3–4 such washings usually suffice. In the following, unless otherwise specified, a starting batch of 10 g may be assumed). With each such washing/centrifugation cycle, as the solution becomes less acidic, it is observed that the supernatant solution (following centrifugation) which was clear on the first cycle, becomes darker. The nearly neutral solution is completely black, remaining black even if longer centrifugation times are used.

Experiments with microscale filtration and electron microscopy (SEM, TEM) of the dark supernatant and the sediment showed all the SWNT to be contained in the sediment covered with a thick coating which consists of the acid decomposition products, along with other liberated species (for example, fullerenes). Carboxylated carbons are a known decomposition product of nitric acid oxidation of carbonaceous material [8]. These are small polycyclic aromatic sheets, edge-terminated with carboxyl groups as well as larger, more cross-linked structures. By virtue of their de-protonation, these carboxylic acids acquire a charge which results in their mutual repulsion, as well as a hydration shell and a consequent solubility in neutral and moderately basic aqueous solutions. The black coloration of the supernatant solution following the later centrifugations is the fraction of this decomposition product having a very high solubility in the nearly neutral aqueous solution.

This solubility provides the means for removal of the bulk of this impurity: filter washing with mildly basic solution. For small material batches, vacuum filter washing with pH 11 NaOH solution on 3–5-μm pore filter membrane suffices. During the filtration, however, the retained SWNTs pack together to block the filter membrane pores. As this SWNT filter cake thickens, the permeation rate of the NaOH solution slows dramatically. If the amount of material exceeds 3 mg/cm^2 of filter surface area this method of washing becomes prohibitively slow.

Fortunately, a standard method for overcoming this problem exists: hollow-fiber, cross-flow filtration (CFF). In hollow-fiber CFF, the filtration membrane takes the form of a hollow-fiber, the wall of which is permeable to the solution (in a range of available pore sizes). The filtrate is pumped down the bore of the fiber at some head pressure from a reservoir and the major fraction of the fast flowing solution which does not permeate out the sides of the fiber is fed back into the same reservoir to be cycled through the fiber repeatedly. The fast hydrodynamic flow down the fiber bore (cross flow) sweeps the membrane surface preventing the build up of a filter cake. A second reservoir contains a buffer solution which is used to make up the filtrate-reservoir solution volume lost to permeation through the fiber wall. Commercially available hollow-fiber cartridges can contain hundreds of hollow fibers potted into an integrated housing. Thus, not only does the method avoid the formation of a permeation-rate-limiting filter cake, but cartridges are available for which the membrane surface areas are measured in square meters.

For SWNT purification in our laboratory-scale CFF system (mini-Kros®, Spectrum, Laguna Hills, CA) the cartridge contains fibers of mixed cellulose ester having a diameter of 0.6 mm, 200-nm pores, and 0.56 m^2 of surface area (M22M 600 01N, Spectrum). Earlier, small-scale experiments using vacuum filtration washing demonstrated that once the acid decomposition product was removed the SWNT ropes became hydrophobic and flocculated out of aqueous solution. This clumping of the material, as the impurity was removed, was found to greatly impede the filtration efficiency. To circumvent this problem a non-ionic surfactant, Triton X-100 (Aldrich, Milwaukee, WI), is added both to the filtrate in the system reservoir and to the buffer solution.

In a typical filtration the (post-acid treatment) solids are dispersed in 1.8 l of pH 10 NaOH solution containing 0.5 vol.% Triton-X 100 by ultrasonic agitation (in a bath sonicator) for $\approx$ 1 h. The buffer solution similarly consists of 40 l of pH 10 NaOH solution containing 0.2 vol.% Triton-X 100. Upon introduction of the filtrate into the CFF reservoir, the pump speed is adjusted to produce a head pressure of 5–6 psi. With a flow control valve added to the permeate outlet side of the system for this purpose, the permeation rate is limited to $\approx$ 70 ml/min. Without this valve a filter cake tends to form and clog the filter, despite the cross flow. At this permeation rate the filtration is completed in $\approx$ 10 h. To remove the salt a further $\approx$ 10 l of deionized water can be run through as the buffer solution. When filtration is complete, clamping off the buffer line and opening a vent permits concentration of the SWNT into $\approx$ 200 ml of solution (see "Note added in proof").

To assay the purification quality and yield, a known volume of the agitated solution (to equally disperse the tubes)

can be collected, followed by vacuum filtering off the liquid through a PTFE membrane (Millipore LS, 5-μm pore). To remove the residual surfactant, washing with methanol is effective. If a sufficiently thick SWNT layer is formed, it may readily be peeled off the membrane to produce a freestanding mat which we call "bucky paper". Figure 3a is a SEM image showing the surface of a piece of bucky paper at this stage of the purification. Figure 3b shows the 4″ apparatus raw material which this started from. The poorer raw starting material was used to demonstrate the efficacy of this process. The weight of the bucky paper and the volume ratios of the sampled volume to the total solution volume permits determination of the mass yield. This is typically 10%–20% depending upon the initial raw material quality.

Despite the dramatic improvement in the SWNT purity, high-resolution TEM images at this stage show the material to still contain a significant quantity of impurities. In order to remove these our approach has been to use successively more oxidizing acid treatments. These are sufficiently reactive to attack the SWNT from the sides so the reaction times are kept much shorter. The first of these is a (3:1) mixture of sulfuric (98%) and nitric (70%) acids (typically 500 ml) stirred and maintained at 70 °C in an oil bath for 20–30 min. This is followed by another CFF cycle as described above. The final "polish" is done with a 4:1 mixture of sulfuric acid (98%) and hydrogen peroxide (30%) following the same procedure as with the sulfuric/nitric mixture. TEM imaging at this stage reveals the SWNT to be largely free of impurities, never theless, as shown below one final step is necessary to obtain our best purified bucky paper: a vacuum bake to 1200 °C.

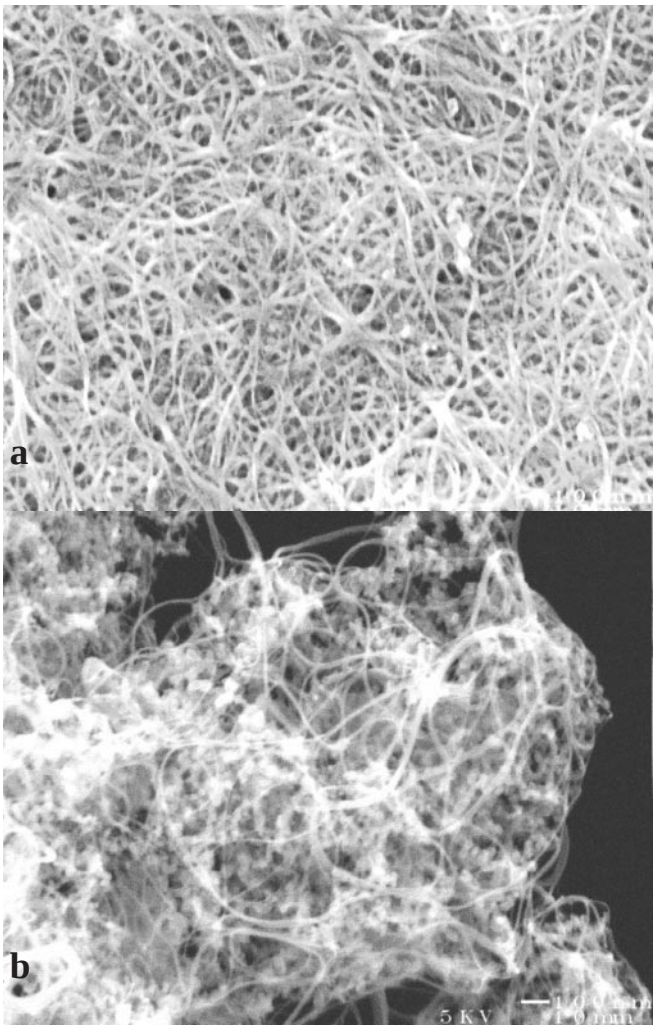

Fig. 3. a SEM image of the surface of bucky paper after the first cross-flow filtration step. **b** SEM image of the 4″ material shown in **a** prior to purification (raw material)

3 Characterization

3.1 TEM

TEM images from purified samples are representative of average behavior since inhomogeneities in the starting material are removed by the extensive mixing occurring during purification. The significant TEM finding (supported by XRD and Raman below) is that the diameter distributions differ in samples from the two systems. Diameter measurements were performed on rope sections parallel to the electron beam (on ropes which curved up through the focal plane) which afford effectively cross-sectional views of the tubes (Fig. 4). To abundantly generate such views for measurement, a small piece of bucky paper was affixed to the TEM sample rod with a torn edge centered in the aperture, followed by wetting with a drop of methanol. At these torn edges, many ropes have been pulled out in a direction perpendicular to the tear. The surface tension of the methanol, as it evaporates, causes these ropes to curl back on themselves. Some fraction of these curve in the appropriate plane to provide images useful for diameter measurement.

To facilitate the diameter determination of many SWNT for good statistics, a routine was written (in Matlab) which allowed a circle to be visually overlaid onto a nanotube wall

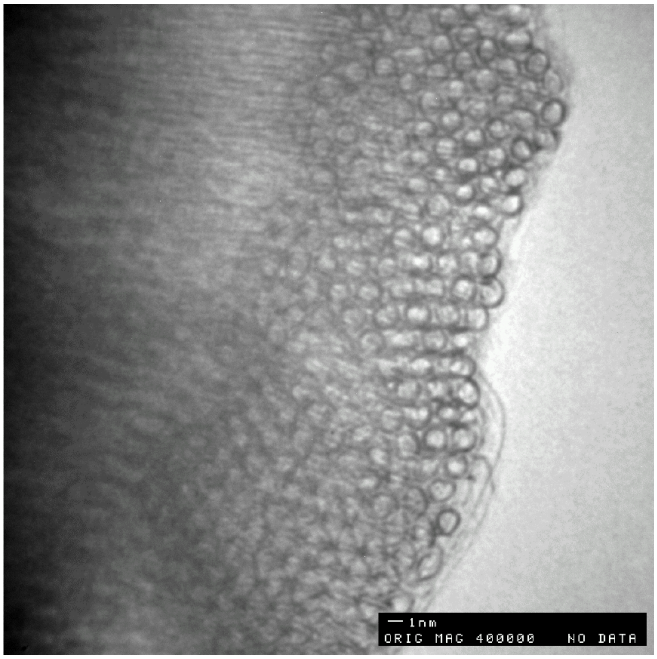

Fig. 4. Cross-sectional view of a SWNT rope permitting direct measurement of nanotube diameters. Measurements were only made on those tubes for which the tube wall was unambiguously distinct in the image

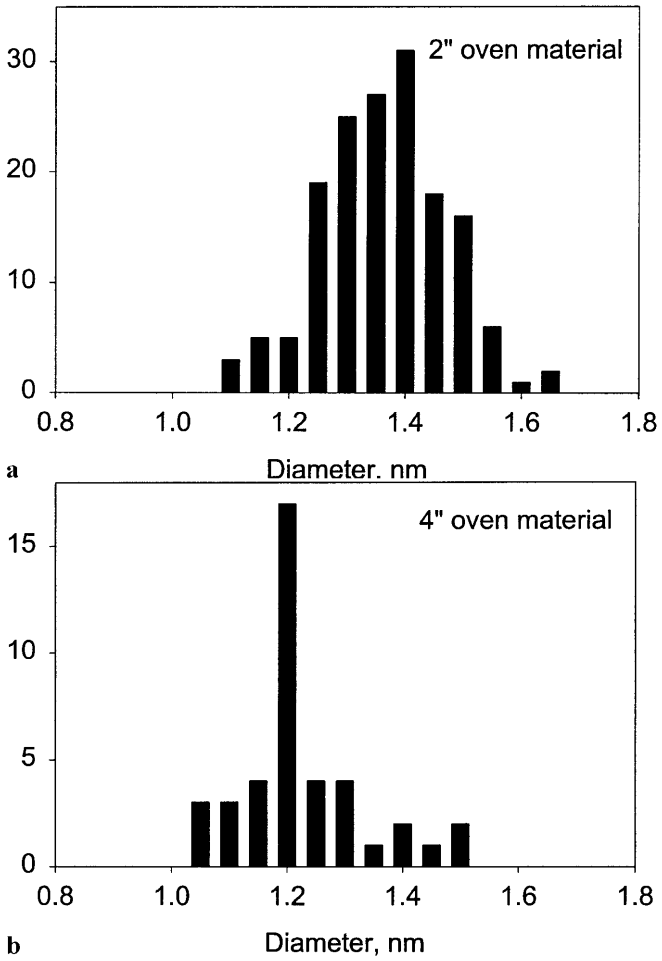

Fig. 5. a The diameter distribution of SWNT made in the 2″ system (1200 °C). **b** The diameter distribution of SWNT made in the 4″ system (1100 °C)

cross section. The routine subsequently generated a least-squares fit of the circle's position and diameter adjusting its perimeter to fall within the center of the nanotube wall. This procedure is estimated to have a relative accuracy of ± 0.05 nm, and an absolute accuracy of ± 0.1 nm.

Figures 5a, b show the diameter distributions obtained in this manner from materials made in the 2″ and 4″ systems, respectively. Evidently, the materials made under the distinct conditions encountered in these systems cause a change in the diameter distributions such that the peak in the 4″ apparatus material is now at ≈ 1.2 nm rather than the ≈ 1.4 nm obtained in the 2″ apparatus. The move to the 4″ system involved several dramatic changes and while it might be conjectured which of these plays the dominant role in effecting this diameter distribution shift, results discussed below strongly implicate the furnace temperature.

3.2 X-ray diffraction

X-ray diffraction was performed in order to determine the effects of chemical treatment and annealing on the nanotubes and their crystalline organization, to follow the evolution of impurity phases throughout the process, and to obtain another estimate of the diameter distribution. We used a powder diffractometer consisting of a sealed Cu tube operating at 1 kW, flat HOPG monochromator, slit before the sample, a curved "linear" detector (250 cm radius) covering 120 degrees in 2-theta and a 4096-channel MCA. Beam divergence was 0.1° FWHM, about 5 times less than the width of the observed diffraction peaks. Samples were prepared as thin freestanding bucky papers 1 cm × 1 cm, mass 1–2 mg. These were mounted at (fixed) grazing incidence. The $1/e$ absorption length for carbon at the density of SWNT material, 0.05–0.15 g/cm^3, is > 2 cm so absorption corrections are negligible even at grazing incidence. Background-corrected diffractograms of rope lattices were compared with model calculations assuming a triangular lattice, homogeneous cylinders of charge and finite widths of peaks in the structure factor $S(Q)$. The width was chosen to match the sharpest fitted peak; it corresponds to a coherence length of 10 nm, or 25 SWNT per rope crystallite.

Figure 6 compares the raw X-ray data for as-grown, acid-purified and acid-purified plus vacuum-annealed material prepared in the 2″ apparatus. The baseline for the first two has been shifted up by 20 000 counts for clarity. The as-grown profile is dominated by diffuse scattering with a broad maximum near 25°, a typical signature of amorphous carbon. In addition we observe two distinct but broad peaks at higher angles, labeled by (*), which can be assigned to the 111 and 200 reflections of 3-nm crystallites of mixed Ni/Co catalyst. Reflections from the rope lattice are evident, especially the first-order peak at 6°. Notably absent is a sharp feature at 27° signaling the absence of graphite, onions, and capsules in significant amounts, distinctly different from previous results [1].

The acid treatment greatly reduces the diffuse background and nearly eliminates the catalyst peaks (middle curve Fig. 6), in agreement with TEM observations. Curiously, we now see distinct reflections labeled by (+) which indicate the presence of 20-nm crystallites of C_{60}. Fullerenes are present in the as-grown material and the cage structure is known to survive more oxidizing acidic conditions than those used here [9]: evidently the residual fullerenes left after the filtration steps have formed small crystallites. The first-order rope lattice peak is diminished in intensity at this stage of the process.

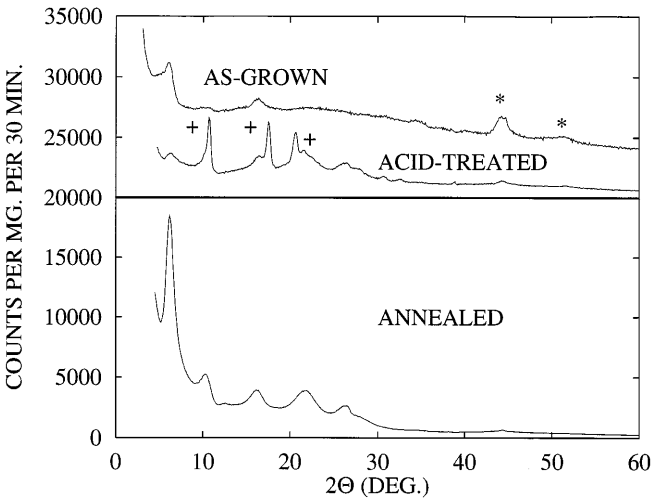

Fig. 6. Raw X-ray data for 2″ SWNT material. TOP (zero shifted to 20 000 for clarity): as-grown and acid-treated material. (*) indicate peaks from Ni/Co catalyst and (+) are indexable as fcc C60. BOTTOM: after final vacuum anneal

Table 1. Analysis of X-ray profiles from two samples (2″, 1200 °C growth and 4″, 1100 °C growth). SWNT diameters 1.36 nm and 1.41 nm

hk	Calc. for D=1.36		Calc. for D=1.41		Obs. low-Q		Obs. high-Q	
	int	Q	int	Q	int	Q	int	Q
1,0	100	0.453	100	0.439	100	0.453	100	0.430
1,1	15	0.722	13	0.695	35	0.733	5	0.685
2,0	6	0.895	7	0.866		NA		NA
2,1	18	1.132	16	1.093	12	1.159	9	1.122
2,2	5	1.497	4	1.446	10	1.510	4	1.457
3,1	8	1.553	8	1.500	19	1.570	6	1.510
3,2	3	1.895	3	1.835	2	1.869	9	1.849
4,0	1	1.732	1	1.676		NA		NA
4,1	3	1.982	3	1.918		NA		NA

The bottom curve shows the acid-purified material after a 1200 °C vacuum annealing (14 h, 1×10^{-6} Torr). The C_{60} has been sublimed out, there remains only a trace of the Ni/Co 111, and the rope lattice is now very well defined. Positions and relative intensities agree generally with our previous measurements on material purified only by vacuum annealing [1]. Tests on small flakes with a strong permanent magnet confirm that most of the magnetic impurities are gone from the final product. Small-angle scattering is still very intense, despite the 3-fold increase in macroscopic density. Using the intensity of the mass-normalized first-order rope peak as a measure of crystalline fraction, we find a sequence 20:5:100 for the as-grown, acid-purified, and subsequently annealed materials, respectively.

X-ray profiles from two samples (2″, 1200 °C growth and 4″, 1100 °C growth) were analyzed in detail. The symbols in Fig. 7 are the background-subtracted data for the 1200 °C sample. The first strong peak is notably asymmetric, the tail on the high-Q side suggesting a second component. Thus the profile was fitted by a series of Gaussians chosen to simulate coexistence of two distinct triangular lattices. The combined fit is shown as the solid curve, and the positions of the component peaks (dashed curves) are compared with peak positions (vertical bars) calculated for triangular lattices with SWNT diameters 1.36 and 1.41 nm, and a 0.32-nm van der Waals inter-tube spacing. The agreement in positions is excellent (part of the intensity near 1.85 Å^{-1} could be due to a trace of graphitic onions). A more detailed comparison of positions and integrated intensities for the two phases is given in Table 1. The overall agreement is very good. In particular, peaks predicted to be the weakest are not observed; the $(2, 2/3, 1)$ doublet centered at 1.5 Å^{-1} is well reproduced, and the general trend in relative intensities is accounted for. Discrepancies between experiment and model could be due to slight flattening of tubes, incomplete coordination near the periphery of the rope crystal, minor admixtures of tubes with nearly the same diameters, etc. We conclude that the crystalline part of the sample consists mainly of two phases in which tubes of diameters differing by 0.06 nm crystallize separately rather than as a solid solution or alloy. Tubes of intermediate diameters may also be present, but we can rule out significant "crystals" of tubes of smaller than 1.36 nm or larger than 1.41 nm; such tubes may be present as individuals or very small nanocrystals which are not detected by X-ray diffraction. Overall, the mean diameter is 1.4 nm, in good agreement with TEM observation.

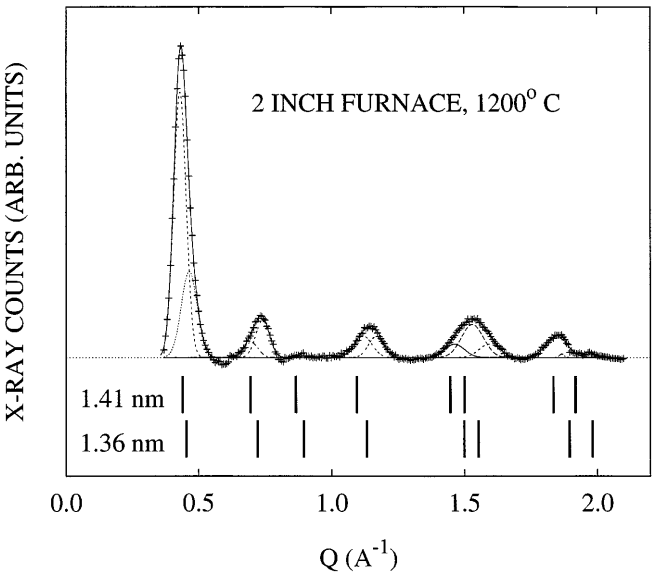

Fig. 7. Gaussian fits to background-subtracted data from annealed 2″ material. (++++) are the data; the solid line is the composite fit and the dashed lines are Gaussians with fixed 0.06 Å^{-1} FWHM. Tick marks below indicate the expected positions from triangular lattices of 1.41-nm and 1.36-nm-diameter tubes, accounting for particle size broadening and the circular form factor

Figure 8 shows a similar analysis for purified material from the 4″, 1100 °C furnace. The composite (observed) peaks are notably shifted to higher Q, indicating a smaller mean diameter. For this sample, the fit implies a somewhat broader diameter distribution since various fitted peaks line up with the vertical bars for 1.22, 1.29 and 1.36-nm tubes. Here the mean of the crystalline material is roughly 1.3 nm, in reasonable agreement with TEM which indicates 1.2 nm.

3.3 Raman

Raman spectra were collected using (i) the 488 nm or 514.5 nm excitation from an Ar ion laser in the backscattering geometry and a HR460 SPEX monochromator equipped with a liquid-nitrogen-cooled CCD detector and (ii) the 1064 excitation from a Nd:YAG laser using the Bomem DA3 Fourier transform spectrometer.

The most intense lines in the spectrum of as-grown 2″ material are the A_g modes at 186 cm^{-1} and 1593 cm^{-1}. After acid treatment, both are up-shifted by 4 cm^{-1}, while the original mode frequencies are recovered after high-temperature annealing. Graphite intercalated with nitric acid (as well as other oxidants) exhibits a similar upshift of the corresponding modes [10]. This analogy lends support to the idea that

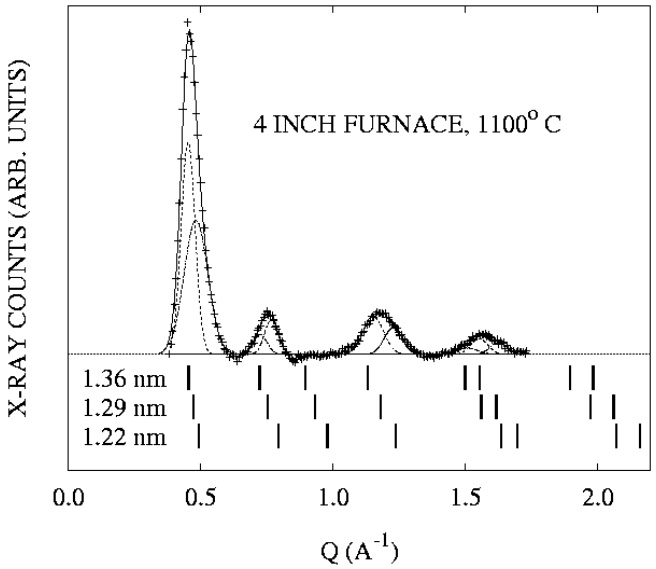

Fig. 8. Similar to Fig. 7 for 4″ material. Note the overall shift to smaller diameters, which we associate with the lower growth temperature (1100 °C vs. 1200 °C in Fig. 7). Note also a possibly broader diameter distribution. The fit is truncated at 1.7 $Å^{-1}$ due to the presence of graphite (002) at 1.86 $Å^{-1}$

in the acid-treated sample, acid molecules are oxidatively intercalated into the rope lattice. This process is apparently reversible since the original Raman frequencies are recovered after the 1200 °C vacuum anneal.

A curious result in these spectra is that whereas the raw material does not exhibit a C_{60} peak, the acid-purified samples do show the associated line at 1469 cm^{-1} (that disappears again after the high-temperature anneal, which sublimes the small fullerenes away). High-pressure liquid chromatography performed on toluene extractions of raw material typically show 5–10 wt.% C_{60}. The surprise is that Raman is apparently not sensitive to the C_{60} known to exist in the raw material. C_{60} was not detected by XRD in the raw material, but XRD requires a minimum crystallite size. Raman has detected C_{60} in previous raw samples made by the PLV process. The present result suggests either dramatic inhomogeneities in the raw sample, and/or that much of the C_{60} exists as an adduct, which modifies the resonant enhancement responsible for the strong Raman signal from pristine C_{60}.

Raman scattering from SWNT bundles has been shown experimentally [11] and theoretically [12] to be a resonant process associated with optical transitions between the one-dimensional states in the electronic band maxima and minima. Raman lines were assigned to the diameter-dependent vibrational mode frequencies ($d < 1.5$ nm). In Fig. 9, we display the low-frequency region of the Raman spectrum for the purified SWNT samples made in the 2″ and 4″ furnaces where resonantly enhanced, diameter-dependent radial-breathing modes are expected. As the data in the figure indicate, it is necessary to use several excitation wavelengths to determine all the radial-mode frequencies. These spectra clearly show the strong resonance effects, i.e., peak shifting and intensity changes as discussed in [11]. Using a force-constant model and the experimentally derived C–C force constants for planar graphite the radial-breathing mode-frequencies for all types of SWNTs

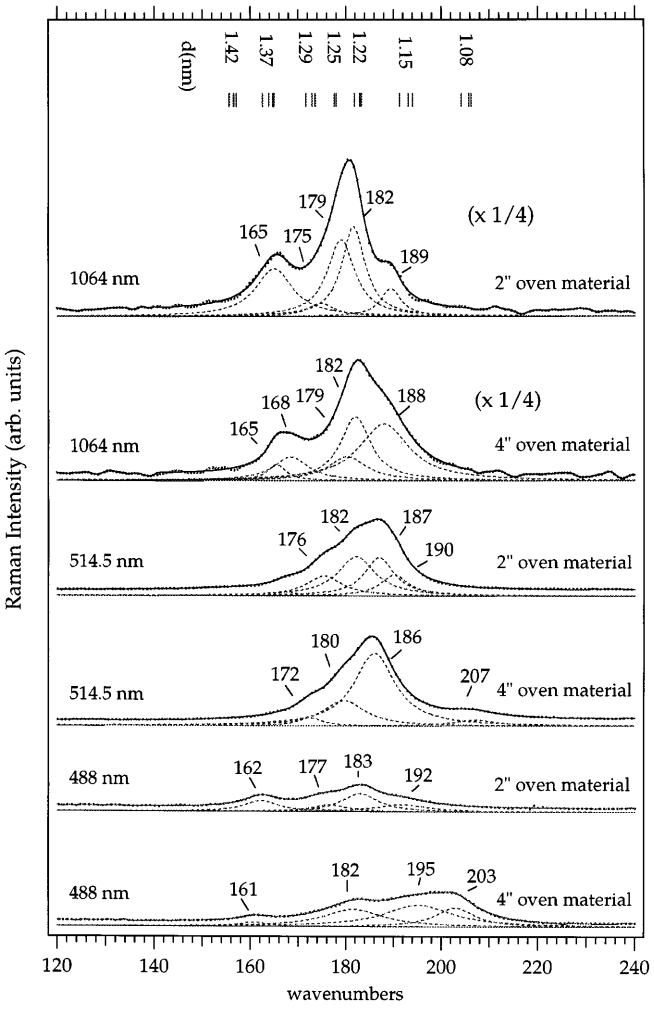

Fig. 9. Raman spectra in the vicinity of the radial mode frequency for the 2″ and 4″ material collected using the indicated excitation frequencies. Vertical bars represent the positions of the calculated radial mode frequency for zigzag, armchair and chiral SWNTs. Individual Lorentzians are also indicated in the figure (see text)

(zigzag, armchair, and chiral) have been obtained [6]. The calculated frequencies were found to be inversely proportional to the tube diameter and are well described by the function $\omega_r(\mathrm{cm}^{-1}) = 223.75/d(\mathrm{nm})$, where d is the tube diameter and ω_r is the radial mode frequency. These calculations showed that ω_r is only sensitive to the tube diameter and not sensitive to the helicity of the SWNT. Thus, smaller diameter tubes are expected to exhibit relatively higher radial-mode frequencies. Relevant calculated frequencies are indicated by vertical bars in the figure.

Individual Lorentzians (dashed curves) were obtained from a lineshape analysis and their peak positions can be used to determine what SWNT diameters (within a range dictated by the natural Raman line widths) are present in the sample. The data indicates that at least five different tubes are present in the 2″ and 4″ furnace samples. Bandow et al. [6] systematically showed that the SWNT diameter distribution in PLV-grown material shifts to larger diameters with increasing furnace temperature. In that work, at least 12 distinct diameters were found in samples prepared at 4 different growth temperatures up to 1000 °C. In corroboration of those

findings and extending the trend to higher temperature, the Raman data here shows that the sample produced at 1200 °C contains, on average, larger diameter tubes than those present in the sample produced at 1100 °C. This systematic increase of average SWNT diameter with growth temperature will have to be addressed in any viable model of SWNT growth.

3.4 Thermo-gravimetric analysis

TGA data were recorded using a TA Instruments STD-2960 DTA-TGA analyzer. In all experiments ramp rates were 5 °C/min to 800 °C following a 2-h hold at 200 °C to remove moisture from the nominally 2-mg sample (contained in an alumina boat). In one experiment the atmosphere was 0.1% oxygen in flowing argon, otherwise the atmosphere was flowing dry air. Flow rates were 100 sccm.

Figure 10a shows data recorded in flowing air for raw SWNT material (○) and material from the same batch which had been vacuum baked at 1200 °C for 14 h (□) prior to burning in the TGA. The high-temperature bake evidently pushes the onset of burning for the raw material from ≈ 360 °C to ≈ 440 °C. Figure 10b shows the behavior of the SWNT material after purification. The (○) curve is for material purified but not vacuum baked displaying a burning onset of ≈ 400 °C. The (□) curve is for purified material vacuum baked at 1200 °C for 14 h which has pushed the burning onset to ≈ 600 °C. The (△) curve is for purified, unbaked SWNT recorded in the low oxygen partial pressure atmosphere, which shows that the major fraction of the sample begins burning at ≈ 600 °C.

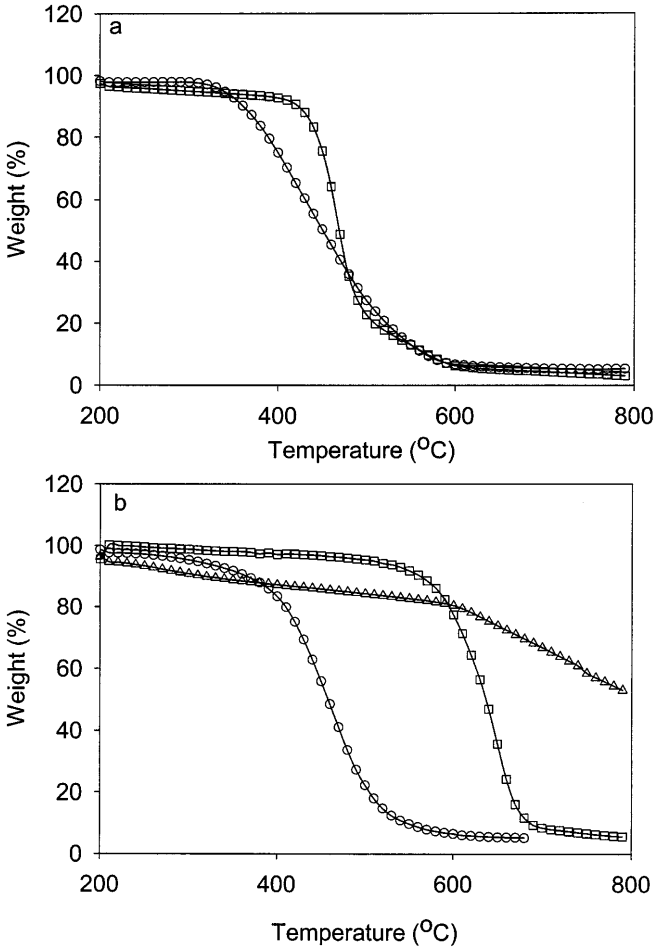

Fig. 10. a TGA data in air of raw SWNT material (○) and the same material which was vacuum baked at 1200 °C for 14 h (□). **b** TGA data in air of purified SWNT material which has (○) and has not (□) been vacuum baked as above. The curve marked (△) is unbaked, purified material run in a 0.1% oxygen (argon balance) atmosphere. See text for discussion

The last experiment, in the oxygen-poor atmosphere, serves to clarify why the unbaked, purified sample burns at the lower temperature. A two-component system will often burn at the lower temperature onset because the exothermic reaction of this component can initiate burning of the second fraction. By throttling back the oxygen partial pressure, the heat released when the first component goes is correspondingly reduced, preventing it from initiating the burn of the second component. Evidently the unbaked purified sample contains a small fraction of a remaining impurity which begins burning at 400 °C and, in air, takes the SWNT with it when it goes.

The experiments demonstrate that the true ignition temperature of SWNT is ≈ 600 °C. This is significantly higher than the reported burning temperature of C_{60} (425 °C) [13], but lower than that of multiwalled carbon nanotubes (≈ 700 °C) [14] and highly graphitized carbon fibers (up to 800 °C) [15]. This intermediate burning temperature of SWNT is consistent with their relative conformational strain compared with the strain in these other carbon polymorphs.

3.5 Resistivity

Four-point resistivity measurements were made using pressure contacts and high-pressure Ar in a Joule–Thompson cold finger cryostat. We studied SWNT grown in the 2″ furnace at 1200 °C. The directionally averaged bulk resistivity, ϱ, was measured for rectangular pieces 2–4 mm wide and 8 mm long. Thickness was calculated from the sample mass and area and an assumed microscopic density of 2 g/cm^3, the latter in an attempt to approximately account for the large porosity.

In Fig. 11, the temperature dependence of ϱ from 90 K to 550 K, shows some unexpected evolution with processing. The ≈ 25-fold decrease in absolute value by chemical purification appears sensible intuitively, while the smaller but significant increase by $\approx 2-4$ upon annealing is curious. More importantly, the temperature dependence changes sign after annealing. $R(T)$ is strongly metallic for the as-grown material, with positive $\mathrm{d}\varrho/\mathrm{d}T$ persisting down to at least 90 K (previous experiments on non-purified, vacuum-annealed samples showed a crossover to negative $\mathrm{d}\varrho/\mathrm{d}T$ at ≈ 200 K [1]). $R(T)$ remains metallic after acid treatment, but the slope changes sign after vacuum-annealing the purified material.

The fact that both bucky papers exhibit lower absolute ϱ than the raw material can be ascribed at least in part to improved inter-tube contacts, similar to what happens with hydrostatic pressure (Bozhkol, this issue). This is because the vacuum filtration compacts the SWNT resulting in a substantially higher macroscopic density for bucky papers compared with the raw material (15 mg/cm^3 vs. 5 mg/cm^3). More difficult to explain is the change in the

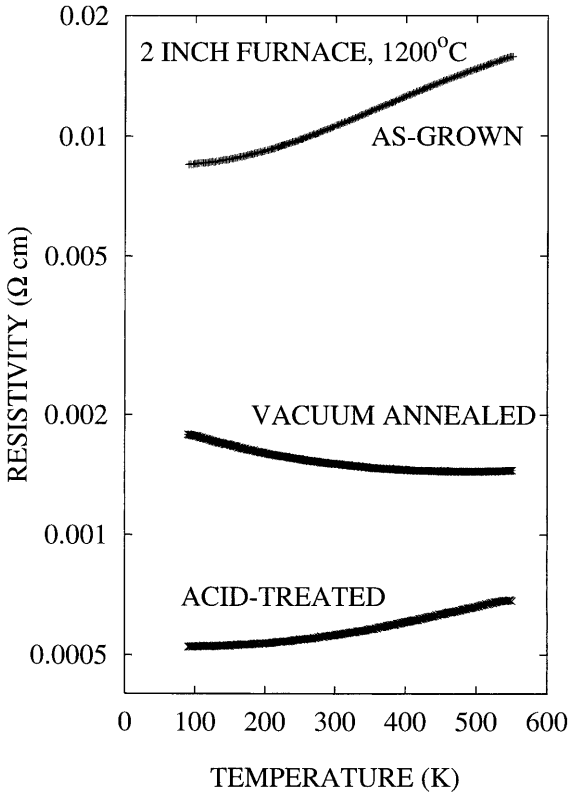

Fig. 11. Four-probe resistivity vs. temperature for 2″ material. The acid purification results in a ≈ 25-fold reduction in ϱ with little change in temperature dependence. Vacuum annealing increases ϱ somewhat and the T dependence changes from metallic to non-metallic (see text)

temperature dependence, from metallic behavior in the raw and un-annealed samples to non-metallic in the final annealed sample. The X-ray data suggests that the latter should come closest to the intrinsic behavior of well-ordered, albeit randomly oriented, rope crystallites while the former no doubt contain large fractions of isolated tubes or very small crystals. Again the correlation with high pressure data is intriguing: $\mathrm{d}R/\mathrm{d}T$ of as-grown material becomes negative above 10 kbar (Bozhkol). It is tempting to associate both behaviors (pressure and purification/annealing) with density-induced changes in morphology. A possible explanation suggested by recent calculations [16] is that tube–tube interactions (enhanced by increased crystallinity in the present annealed samples or by uniform compression in the pressure experiments) leads to the opening of a pseudo-gap in the density of states and a crossover from a metallic to a semi-metallic ground state.

4 Summary and conclusion

The dual PLV process for SWNT production has been scaled up to synthesize 10 g/day of ≈ 45 vol.% material. In combination with our readily scalable purification method (yield 10–20 wt.%) the production of g/day quantities of high-quality material is in hand. Characterization of this material by SEM, TEM, XRD, Raman scattering, and TGA show it to be highly pure. These successes permit the production of gram-scale quantities of high-purity SWNT on a daily basis. This opens the way for a host of material properties studies which were previously inconceivable for want of adequate supplies of sufficiently pure SWNT. The purification process should be of particular interest in light of recent reports of a large-scale, arc-based process for SWNT production [17].

Acknowledgements. Support for this work was provided by (i) at Rice: NSF Grant #DMR 95-2251, the Advanced Technology Program of Texas Grant #003604-047, and the Welch Foundation Grant #C-0689; (ii) at UPenn: The Department of Energy Grant #DE-FC02-86ER45254; and (iii) at UKentucky: the Center for Applied Energy Research, and NSF Grant #OSR-94-52895.

Note added in proof

Continuing work with the cross flow filtration system has revealed that a crucial step in obtaining the levels of SWNT purification described in the text is the frequent reversal of the CFF pump direction for a few seconds during the filtration run (the permeate outlet and buffer inlet lines should be clamped off during such reversals). Within a few minutes of starting the filtration, a thin nanotube layer (a gel layer in the parlance of separation science) forms on the surface of the hollow fiber membrane which blocks the passage of nanoparticles out through the pores. Each reversal forces the gel layer into the fast moving cross flow where it can be swept away, leaving the membrane pores accessible to the nanoparticles. The occurrence of such reversals may readily be automated.

References

1. A. Thess, R. Lee, P. Nikolaev, H. Dai, P. Petit, J. Robert, C. Xu, Y.H. Lee, S.G. Kim, A.G. Rinzler, D.T. Colbert, G.E. Scuseria, D. Tomanek, J.E. Fisher, R.E. Smalley: Science **273**, 483 (1996)
2. N. Hamada, S.I. Sawada, A. Oshiyama: Phys. Rev. Lett. **68**, 1579 (1992); J.W. Mintmire, B.I. Dunlap, C.T. White: Phys. Rev. Lett. **68**, 631 (1992); R. Saito, M. Fujita, G. Dresselhaus, M.S. Dresselhaus: MRS Symp. Proc. **247**, 333 (1992)
3. K. Tohji, T. Goto, H. Takahashi, Y. Shinoda, N. Shimizu, B. Jeyadevan, I. Matsuoka, Y. Saito, A. Kasuya, T. Ohsuna, K. Hiraga, Y. Nishina: Nature **383**, 679 (1996)
4. K. Tohji, H. Takahashi, Y. Shinoda, N. Shimizu, B. Jeyadevan, I. Matsuoka, Y. Saito, A. Kasuya, T. Ohsuna, S. Ito, Y. Nishina: J. Phys. Chem. B **101**, 1974 (1997)
5. S. Bandow, A.M. Rao, K.A. Williams, A. Thess, R.E. Smalley, P.C. Eklund: J. Phys. Chem. B **101**, 8839 (1997)
6. S. Bandow, S. Asaka, Y. Saito, A.M. Rao, L. Grigorian, E. Richter, P.C. Eklund: submitted to Phys. Rev. Lett.
7. S.C. Tsang, Y.K. Chen, P.J.F. Harris, M.L.H. Green: Nature **372**, 159 (1994)
8. K. Kinoshita: *Carbon Electrochemical and Physicochemical Properties* (Wiley, New York 1988)
9. L.Y. Chiang, J.W. Swirczewski, C.S. Hsu, S.K. Chowdhury, S. Cameron, K. Creegan, J. Chem. Soc., Chem. Commun. **24**, 1791 (1992)
10. See for example, review article by M.S. Dresselhaus, G. Dresselhaus: Adv. Phys. **30**, 139 (1981)
11. A.M. Rao, E. Richter, S. Bandow, B. Chase, P.C. Eklund, K.A. Williams, S. Frang, K.R. Subbaswamy, M. Menon, A. Thess, R.E. Smalley, G. Dresselhaus, M.S. Dressehaus: Science **275**, 187 (1997)
12. E. Richter, K.R. Subbaswamy: Phys. Rev. Lett. **79**, 2738 (1997)
13. L.S.K. Pang, J.D. Saxby, S.P. Chatfield: J. Phys. Chem. **97**, 6941 (1993)
14. P.M. Ajayan, T.W. Ebbesen, T. Ichihashi, S. Iijima, K. Tanigaki, H. Hiura: Nature **362**, 522 (1993)
15. M.S. Dresselhaus, G. Dresselhaus, K. Sugihara, I.L. Spain, H.A. Goldberg: *Graphite Fibers and Filaments* (Springer, New York 1988)
16. P. Delaney, H.J. Choi, J. Ihm, S.G. Louie, M.L. Cohen: Nature **391**, 466 (1998)
17. C. Journet, W.K. Maser, P. Bernier, A. Loiseau, M.L. Delachapelle, S. Lefrant, P. Deniard, R.S. Lee, J.E. Fischer: Nature **388**, 756 (1997)